DEUTSCHES ELEKTRONEN — SYNCHROTRON

DESY 95-042
March 1995

Results from the ZEUS Experiment at HERA

B. Löhr

Deutsches Elektronen-Synchrotron DESY, Hamburg

ISSN 0418-9833

NOTKESTRASSE 85 - 22603 HAMBURG

To be sure that your preprints are promptly included in the
HIGH ENERGY PHYSICS INDEX,
send them to (if possible by air mail):

DESY **Bibliothek** **Notkestraße 85** **22603 Hamburg** **Germany**	**DESY-IfH** **Bibliothek** **Platanenallee 6** **15738 Zeuthen** **Germany**

DESY 95-042
March 1995

ISSN 0418-9833

Results from the ZEUS Experiment at HERA

B.Löhr
Deutsches Elektronen-Synchrotron DESY, Hamburg

Abstract

Results from analyses of the data taken with the ZEUS detector in 1992 and 1993 are presented. The topics are selected from photoproduction, deep inelastic scattering in neutral and charged currents reactions, and from large rapidity gap events.

Talk given at the XXII SLAC Summer Institute and Topical Conference,
Stanford, August 1994

1 The ZEUS Detector

ZEUS is a magnetic detector [1] at the electron-proton storage ring HERA. Figure 1 shows a vertical cross section through the detector in the plane which contains the HERA beamline. Protons of 820 GeV collide with electrons of 26.7 GeV in the center of the detector. The interaction point is surrounded by the tracking detector system which consists of a small drift chamber, the vertex detector [2], a large cylindrical drift chamber [3], and transition radiation detectors and planar drift chambers at both ends of the large cylindrical drift chamber. The tracking detector system is placed inside a superconducting solenoid which produces a magnetic field of 1.43 T. The high resolution uranium-scintillator calorimeter [4], which encloses the tracking detector system, consists of three parts : the forward[1] calorimeter (FCAL), the barrel calorimeter (BCAL), and the rear calorimeter (RCAL). The high resolution calorimeter covers the complete solid angle of 4π except for holes of 20 cm $\times$ 20 cm cross section in the FCAL and RCAL to accommodate the HERA beampipe. The inner ZEUS detector is surrounded by an iron flux return yoke. The yoke is instrumented with proportional tube chambers and acts as a backing calorimeter to detect energy leaking out of the high resolution calorimeter. The iron yoke is sandwiched between limited streamer tube chambers to identify and to measure muons. In the forward direction, muon detection is reenforced by additional toroidal magnets and a system of drift chambers and limited streamer tube chambers. The luminosity monitor [5] consists of two small lead-scintillator calorimeters in the HERA tunnel which measure the rate of the Bethe-Heitler process $e + p \rightarrow e' + p + \gamma$ by detecting the scattered electron and the radiated photon. The leading proton spectrometer consists of six stations with silicon strip detectors very close to the proton beam in the HERA tunnel to measure protons scattered under very small angles.

2 Photoproduction Results from ZEUS

When a 26.7 GeV electron collides with a 820 GeV proton in HERA, in most cases it scatters under a small angle Θ_e by emission of a virtual photon which then interacts with the proton, see fig.2.

The virtuality of the emitted photon is given by the sqare of the difference of the four vectors of the incoming electron (k) and the outgoing electron (k') :

$$Q^2 = -q^2 = -(k - k')^2.$$

We are dealing with a photoproduction reaction if $Q^2 \approx 0$. The energy transfer from the electron to the proton in the rest system of the proton is given by :

$$\nu = \frac{2E_p}{m_p}(E_e - E'_e cos\frac{\Theta_e}{2})$$

where E_p and m_p are the energy and the mass of the interacting proton and E'_e is the energy of the scattered electron. Alternatively, the Lorentz invariant variable

$$y = \frac{\nu}{\nu_{max}} \approx \frac{E_e - E'_e}{E_e}$$

[1]The direction of the incident protons is called the forward direction. The ZEUS coordinate system is chosen such that the z axis points forward, the y axis upwards, and the x axis towards the center of the HERA ring.

is used. Another quantity which characterizes the process is the hadronic center of mass energy W which is given by :

$$W^2 = (q+p)^2 \cong 4E_\gamma E_p.$$

For the present beam energies, the electron proton collider HERA is equivalent to a fixed target photoproduction experiment with photon energies up to 48 TeV.

Experimentally, one distinguishes two classes of photoproduction events :

- In *tagged* photoproduction events, the scattered electron is detected in the electron calorimeter of the luminosity monitor. This restricts Q^2 to the range $10^{-7} < Q^2 < 2 \times 10^{-2}\text{GeV}^2$.
- In *untagged* photoproduction events, the scattered electron is not detected. It is detectable in the ZEUS calorimeter for $Q^2 > 4$ GeV^2. For untagged photoproduction events, the median value of Q^2 is ≈ 0.001 GeV^2.

In both cases, the average Q^2 values are very small and it is justified to speak of photoproduction reactions.

2.1 The many faces of the photon

It is well known that in reactions which involve only low transverse momenta the photon behaves like a hadron. At low energies, this feature is sufficiently well described by the vector meson dominance model (VDM) [6]. The photon fluctuates into a vector meson state (ρ, ω, ϕ) which then interacts with the proton. These interactions are elastic vector meson scattering, diffractive scattering with single and double dissociation, and non-diffractive scattering, see fig.3. The final states may contain also high transverse momentum particles.

Photoproduction reactions involving high transverse momenta are supposed to be described by perturbative Quantum Chromodynamics (QCD). In lowest order QCD, there are two ways for the photon to interact with constituents of the proton :

- As shown in fig.4a, the photon couples directly to the electric charge of a quark inside the proton. The whole momentum of the photon is transferred to the scattered quark.
- The photon fluctuates into a hadronic state and only a fraction of this state interacts with the proton. An example is shown in fig.4b. In this case, part of the initial momentum of the photon is carried away by the photon remnant. One calls this a resolved photon interaction.

In higher order QCD, the distinction between direct and resolved processes is not so clear.

2.2 The total photoprodution cross section

In the ZEUS experiment, the total photoproduction cross section was measured using a sample of tagged photoproduction events at an average photon-proton center of mass energy of $< W_{\gamma p} >= 180$ GeV [7]. The major contributions to the total cross section were identified by fitting Monte Carlo models of the various subprocesses to the measured energy distributions in the calorimeter parts (FCAL,BCAL, RCAL). The same models were used to calculate the detector acceptances for the subprocesses. In this way the total as well as the fractional cross

sections for the subprocesses were determined. In the first step, a cross section for the ep reaction was calculated. It is related to the γp cross section by the relation

$$\sigma_{ep} = F_{e\gamma} \cdot \sigma_{\gamma p}$$

where $F_{e\gamma}$ is the known flux factor for the radiation of photons from the incoming electron. The result is :

$$\sigma_{tot}(\gamma p) = (143 \pm 4 \pm 17)\ \mu b.$$

The contributions from the subprocesses are : $(12.7 \pm 1.5 \pm 4.7)$ % for elastic vector meson scattering, $(23.3 \pm 2.7 \pm 4.3)$ % for single diffractive and double dissociative processes, and $(64.0 \pm 0.9 \pm 3.6)$ % for non-diffractive reactions. Figure 5 shows the total photoproduction cross section, measured by ZEUS, together with the measurement of H1 [8] at HERA and measurements at lower $W_{\gamma p}$ values [9]. Also shown are extrapolations of cross section parametrizations by Donnachie and Landshoff (DL) [10] and Abramowicz, Levin, Levy, Maor (ALLM) [11], which are both based on Regge type calculations, as well as a QCD inspired prediction (minijets) [12]. The Regge based extrapolations are in agreement with the ZEUS and H1 measurements. The "minijet" prediction shows a faster rise with $W_{\gamma p}$ which is also compatible with the HERA data.

2.3 Vector meson production

Elastic vector meson production has been observed at ZEUS in various channels in untagged photoproduction events. In fig.6a-d the signals for ρ, ω, ϕ, and J/Ψ production are shown. The analyses are still in progress. Preliminary cross sections are [13]:

for ρ production

$\sigma(\gamma p \to \rho^0 p) = (12.5 \pm 0.7 \pm 2.8)\ \mu b$ for $p_t^2 < 0.5$ GeV^2, $< \mathrm{W}_{\gamma p} >= 70$ GeV,
where p_t is the transverse momentum of the ρ^0.

for J/Ψ production

$$\begin{aligned}
\sigma(\gamma p \to J/\Psi + p \to e^+e^- + p) &= (62 \pm 13 \pm 13)\ nb \text{ at } 40 < \mathrm{W}_{\gamma p} < 75 \text{ GeV} \\
\sigma(\gamma p \to J/\Psi + p \to e^+e^- + p) &= (70 \pm 16 \pm 13)\ nb \text{ at } 75 < \mathrm{W}_{\gamma p} < 140 \text{ GeV} \\
\sigma(\gamma p \to J/\Psi + p \to \mu^+\mu^- + p) &= (48 \pm 12 \pm 14)\ nb \text{ at } 40 < \mathrm{W}_{\gamma p} < 90 \text{ GeV} \\
\sigma(\gamma p \to J/\Psi + p \to \mu^+\mu^- + p) &= (84 \pm 21 \pm 24)\ nb \text{ at } 90 < \mathrm{W}_{\gamma p} < 140 \text{ GeV}
\end{aligned}$$

In case of the J/Ψ cross sections, a yet not determined contribution from proton dissociation is present in the data. All cross sections are corrected for the branching ratios of the J/Ψ decay channels. In fig.7 the ZEUS results are compared to measurements at lower energies [14]. While $\sigma(\gamma p \to \rho^0 p)$ is consistent with a slow rise for $W > 10$ GeV the $\sigma(\gamma p \to J/\Psi + p)$ shows a significant rise.

2.4 Inclusive charged particle p_t distribution

Inclusive charged particle distributions have been determined using a sample of tagged photoproduction events. To ensure precise tracking and good geometrical acceptance charged

particles were required to have transverse momenta $p_t > 300$ GeV/c and pseudorapidities [2] $-1.2 < \eta < 1.4$ ($27.7° < \Theta_{track} < 146.5°$). Preliminary results for the inclusive charge particle p_t distributions have been obtained for non-diffractive events and two samples of diffractive events with average masses of the dissociated system of $< M_x >= 5$ GeV and $< M_x >= 10$ GeV [15]. For these distributions the average γp cms energy is $< W_{\gamma p} >= 180$ GeV. The results are shown in fig.8. At low p_t, the distributions show an e^{-bp_t} behavior with coefficients $b = 4.87 \pm 0.1 \pm 0.08$ for non-diffractive events, $b = 5.19 \pm 0.05 \pm 0.23$ for $< M_x >= 10$ GeV, and $b = 5.61 \pm 0.1 \pm 0.14$ for $< M_x >= 5$ GeV. In the non-diffractive event sample, the distribution shows a clear excess of events at higher transverse momenta. This indicates the presence of hard scattering processes in photoproduction.

2.5 High p_t photoproduction

Hard scattering processes with high transverse momenta in the final state manifest themselves by the appearence of jets. A search for jets was performed with the ZEUS detector [16]. Jets were defined by a cone algorithm [17]. The radius of the cone was chosen to be $R = \sqrt{\Delta\eta^2 + \Delta\phi^2} = 1$ where ϕ is the azimuthal angle. Fig.9a shows the inclusive jet cross section for the kinematical regime $E_t^{jet} > 8$GeV , $-1 < \eta^{jet} < 2$, and $0.2 < y < 0.85$. Fig.9b shows the corresponding η distribution of the found jets. The data are compared to Monte Carlo model calculations using the proton structure function parametrization MRSD- [18] and two different photon structure function parametrizations, GRV [19] and LAC1 [20].

As outlined above, the photon interaction may be direct or resolved. Fig.10 visualizes one possibility of a resolved photon interaction. If two jets are detected in such events, one can determine the fraction x_γ of the photon's momentum which took part in the hard scattering process :

$$x_\gamma = \frac{\sum_{jets}(E - p_z)}{\sum_{cal}(E - p_z)}$$

where E and p_z are the energy and the longitudinal momentum measured in a single calorimeter cell. The longitudinal momentum p_z is calculated from the cell energy and the polar angle of the center of the cell w.r.t. the interaction vertex. Each sum runs over all cells associated with the jets or all cells in the calorimeter respectively. The distribution of measured x_γ values [21] is presented in fig.11. One recognizes a clear peak at high x_γ values coming from direct photon interactions and a rather flat distribution down to low x_γ values which originates from resolved photon processes. Also shown are Monte Carlo simulations of only direct interactions, only resolved processes, and the sum of the two contributions. These simulations describe fairly well the measured data and confirm the above interpretation of the x_γ distribution. Quantitatively one finds for the kinematical region $0.2 < y < 0.7$, $E_T^{jets} > 5$ GeV^2 , and $\eta^{jets} < 1.6$:

$$\sigma_{res} = (21.1 \pm 5.2 \pm 5.7)\ nb \quad \text{and}$$
$$\sigma_{dir} = (9.4 \pm 2.7 \pm 2.7)\ nb\ .$$

In this kinematical range, the resolved photon interactions give the dominant contribution.

[2] The pseudorapidity is defined as $\eta = -ln(tan\frac{\Theta}{2})$. Note that $\Theta = 0°$ is the proton direction. Positive η values correspond to the forward direction.

2.6 Study of the photon remnant

The measured x_γ distribution demonstrates the existence of both direct and resolved photon processes. Fig.12 shows the presence of the resolved component for events with jets in a different way. It shows a scatter plot of the energy measured in the rear calorimeter (E_{RCAL}) versus the pseudorapidity of the most backward going jet (η_{min}). As long as $\eta_{min} < 0$, a clear correlation with E_{RCAL} is visible in the sense that E_{RCAL} increases when η_{min} becomes more negative. However, if $\eta_{min} > 0$, i.e. the most backward jet is going forward, many events remain with energy deposits in the RCAL as high as 15 GeV. These energy deposits are due to photon remnants. To further study the behavior of the photon remnant, events were selected with a total transverse energy of more than 12 GeV measured in the calorimeter outside a cone of 10° in the forward direction. A cluster algorithm was applied to all events and was forced to find three separate energy clusters in addition to the proton remnant (3+1 cluster events) [22]. The clusters were ordered according to their measured tranverse energies in the calorimeter. For each cluster an axis was determined as the direction of the vector sum of the momenta measured in the associated calorimeter cells. The pseudorapidities of the cluster axes were required to be $\eta(3) < -1$ for the third cluster and $\eta(1,2) < 1.6$ for clusters 1 and 2. In order to guarantee that the event was generated by a hard scattering process, the transverse momenta of the clusters 1 and 2 were requested to be $p_t(1,2) > 5$ GeV. These cuts select events in which the third cluster is predominantly the photon remnant. For each cluster, longitudinal and transverse energies w.r.t the cluster axes were calculated as $E_{L,T} = \sum_i E_{L,T}^i$ where the sum runs over the associated calorimeter cells. In fig.13, the average longitudinal and transverse energies $< E_L >$ and $< E_T >$ are plotted versus the cluster energies. The average longitudinal cluster energy $< E_L >$ rises linearly with the cluster energy for all three cluster in the same way. The average transverse cluster energy $< E_T >$ also rises with the cluster energy for all three cluster types in the same way but not as fast as $< E_T >$. One concludes that the photon remnant behaves like a normal jet produced by colored constituents.

3 Deep Inelastic Scattering

Deep inelastic scattering (DIS) for neutral current (NC) events is described in lowest order (naive quark parton model) by the diagram in fig.14 . The incoming electron is scattered by exchanging either a photon or a Z-boson with one of the quarks inside the proton. The incoming quark, carrying the fraction x of the proton's four momentum p, is scattered out of the proton and gives rise to the current jet. The remnants of the proton form a jet which disappears in the forward beampipe.

The kinematics of the reaction is determined by two variables. Commonly used are the negative square of the four momentum transfer Q^2, which is nonzero for DIS events, and the struck quark's momentum fraction x which is given by

$$x = \frac{Q^2}{2q \cdot p}\ .$$

The normalized energy transfer variable y can be expressed in a Lorentz invariant way

$$y = \frac{q \cdot p}{k \cdot p}\ .$$

These three variables are not independent. They are connected with the center of mass energy squared of the ep system $s = (k + p)^2$:

$$xys = Q^2.$$

At HERA, the ep center of mass energy is $\sqrt{s} = 296$ GeV. The virtual photon-proton center of mass energy is $W = \sqrt{(q+p)^2}$. Fig.15 shows the kinematical regime in the Q^2-x plane covered by the ZEUS measurements. The line $y = 1$ is the kinematical limit. The shape of the scatter plot at low x and low Q^2 is determined by the calorimeter acceptance : the scattered electron starts to escape detection in the calorimeter through the rear beampipe hole. Also shown are the kinematical regimes covered by previous fixed target experiments.

The double differential cross section for the production of DIS neutral current events is given in terms of three structure functions F_2, F_L, and xF_3 :

$$\frac{d^2\sigma}{dxdQ^2} = \frac{2\pi\alpha^2}{xQ^4}[(1 + (1 - y)^2) \cdot F_2(x, Q^2) - y^2 \cdot F_L(x, Q^2) + (1 - (1 - y^2)) \cdot xF_3(x, Q^2)].$$

The structure function xF_3 originates from Z-boson exchange, the parity violating weak neutral current contribution. At Q^2 values accessible with sufficient statistics up to now, this contribution is small and generally neglected. In certain kinematical regions, where it cannot be neglected, the data are corrected. The contribution from F_L is small in the kinematical region under study and the data have been corrected for it using perturbative QCD expectations. Thus F_2 gives the cross section for photon exchange. The total virtual photon-proton cross section can be written in terms of the total cross sections σ_T and σ_L for transverse and longitudinal photon proton scattering

$$\sigma_{tot}(\gamma^* p) = \sigma_T(x, Q^2) + \sigma_L(x, Q^2) = \frac{4\pi^2\alpha}{Q^2(1 - x)} \cdot F_2(x, Q^2).$$

3.1 Measurement of F_2

DIS events are identified by the detection of the scattered electron. ZEUS is a hermetic detector, i.e. particles are detected in the full solid angle 4π, except in the beampipe region. Therefore the kinematical variables can be calculated from either the scattered electron, the measured hadronic system, or any combination of them. In the ZEUS analysis two different methods were used :

- Electron method :
  The measured energy E_e' and angle Θ_e of the scattered electron are used. This method gives a good resolution for Q^2 and x in the region of high y.

- Double angle (DA) method [23]:
  Θ_e' and γ_h are used. The hadronic angle γ_h is given by :

  $$cos\gamma_h = \frac{(\Sigma p_x)^2 + (\Sigma p_y)^2 - (\Sigma(E - p_z))^2}{(\Sigma p_x)^2 + (\Sigma p_y)^2 + (\Sigma(E - p_z))^2}.$$

  In the naive quark parton model, γ_h is the angle under which the struck quark emerges. The DA method allows to measure Q^2 and x with good accuracy over the full kinematical region under study and has the advantage of being rather insensitive to the energy scale of the calorimeter measurement. Variables determined in this way are denoted by the subscript DA.

Figures 16a and 16b show the measured F_2 values as functions of x for different Q^2 values [24]. The background from photoproduction events in which electrons or other particles are misidentified as the scattered electrons is of the order of a few percent. In the worst bin it is 12%. Data were corrected for this background bin by bin on a statistical basis.

The prominent feature of the data is the strong rise of F_2 with decreasing x at all measured Q^2 values. This means that the parton density increases at small x.

Perturbative QCD predicts for fixed x the dependence of F_2 on Q^2. The Q^2 dependence of the structure function F_2 is described by the GLAP evolution equation [25]:

$$\frac{dF_2}{dlnQ^2} = \sum_q e_q^2 \frac{\alpha_s(Q^2)}{2\pi} \int_x^1 \frac{dy}{y}[P_{qq}(\frac{x}{y})q(y, Q^2) + P_{qg}(\frac{x}{y})g(y, Q^2)]$$

The quark and gluon distribution functions $q(y, Q^2)$ and $g(y, Q^2)$ describe the probablity to find a quark or gluon with momentum fraction y inside the proton in a reaction at Q^2. P_{qq} and P_{qg} are the splitting functions. $P_{qq}(\frac{x}{y})$ gives the probability to find a quark with momentum fraction x of the proton coming from the splitting (gluon radiation) of a quark with momentum fraction y. P_{qg} gives the probability to find a quark with momentum fraction x from the splitting of a gluon (quark pair production) with momentum fraction y. The splitting functions are calculable in perturbative QCD.

Various authors have parametrized the structure function $F_2(x)$ at some $Q^2 = Q_o^2$ and used the GLAP equation to predict the QCD evolution. The parameters of $F_2(x)$ are then fitted to data used as experimental input at all x and Q^2 values. Several such parametrizations are compared to the ZEUS data in figures 16a and 16b. They differ in the assumptions about the x dependence, in particular about the gluon momentum distribution function $xg(x)$ in the proton at Q_o^2. The following parametrizations are plotted :

- MRSD$_o'$ [26] :
  Input data from fixed target experiments are used. The gluon distribution at small x is assumed to behave like $xg(x) \rightarrow$ const..

- MRSD'$_-$ [18] : The same input is used as for MRSD$_o'$ but the assumption $xg(x) \rightarrow x^{-0.5}$ is made for small x.

- CTEQ2D [27] : Fixed target data plus the HERA 1992 data have been used as input and a gluon distribution $xg(x) \rightarrow x^{-n}$ ($n \approx 0.3$) for small x is assumed.

- GRV-HO [28] : These authors start the Q^2 evolution already from $Q_0^2 = 0.3$ GeV^2 and use valence type distributions for the quarks, the sea, and the gluons.

- GRV-MCH [29] : This is the same as GRV-HO but the charm quark mass is properly taken into account.

The data are best described by parametrizations whith singular gluon distributions at small x, either parametrized or generated dynamically (GRV).

Fig.17 shows the F_2 measurements from ZEUS as functions of Q^2 at different x values. Also shown are data from H1 [30], NMC [31], and E665 [32]. The data are consistent with each other and are well in agreement with the predicted scaling violations, i.e. the variation of F_2 with lnQ^2 at a fixed x. Also plotted are predictions from the MRSD$_o'$ and MRSD'$_-$ parametrizations.

Scaling violations occur through gluon radiation from quarks and quark pair production from gluons. At $x < 10^{-2}$ the latter process dominates the scaling violations. This property

can be used to extract the gluon density from the slope $dF_2/dlnQ^2$ of the proton structure function. Three methods have been used by ZEUS:

- The Prytz method [33] : The quark contribution is neglected at small x and the gluon momentum distribution $xg(x)$ is directly related to the scaling violations. The result for the gluon distribution has been calculated in leading order (LO) QCD and next to leading order (NLO). The corresponding results are:

$$\text{LO} \quad xg(x) = \frac{dF_2(x/2,Q^2)/dlnQ^2}{(40/27)\alpha_s/4\pi}$$

$$\text{NLO} \quad xg(x) = \frac{dF_2(x/2,Q^2)/dlnQ^2}{(40/27+7.96\alpha_s/4\pi)} - \frac{(20/9)(\alpha_s/4\pi)N(x/2,Q^2)}{40/27+7.96\alpha_s/4\pi}.$$

  The function $N(x,Q^2)$ has been calculated by Prytz.

- The EKL method [34] : These authors solve the full GLAP equation in moment space in NLO and NNLO for the gluon contribution. They make the assumption that the singlet part of F_2 and the gluon distribution at small x is of the functional form $F_2 \sim x^{-\omega_o}$ and $xg(x) \sim x^{-\omega_o}$. The value of ω_o is an input parameter and has to be determined from the data.

ZEUS used both methods to extract the gluon distribution from their measured F_2 data [35]. The results are shown in fig.18.

ZEUS performed also a complete fit of the GLAP equation to the data. The resulting gluon distribution is shown in fig.18. The data are compared to extrapolations from the MRSD$'_o$ and MRSD$'_-$ parametrizations. The data suggest a strong rise of $xg(x)$ towards low x. Parametrizations with a flat gluon distribution at small x, like MRSD$'_o$, are disfavored.

The x dependence of F_2 is not predicted by the GLAP equation. For the gluon distribution an x dependence can be derived as a function of Q^2 :

$$\text{GLAP} \qquad xg(x) \sim exp[2\xi(Q_o^2,Q^2)ln(1/x)]^{\frac{1}{2}}.$$

The function $\xi(Q_o^2,Q^2)$ is caculable in perturbative QCD. A different perturbative approach for the QCD evolution of structure functions is the BFKL equation [36]. This results in :

$$\text{BFKL} \qquad xg(x) \sim x^{-\lambda} \;\; ; \;\; \lambda = (3\alpha_s/\pi)4ln2 \approx 0.5.$$

From a comparison of the ZEUS data with the structure function parametrizations (e.g. MRSD$'_-$) one sees that the data at low x and $Q^2 > 35$ GeV^2 are compatible with

$$F_2 \approx a + \frac{b}{\sqrt{x}}.$$

Using the relation $W^2 \approx Q^2/x$ one can write

$$F_2 \approx a + b\frac{W}{Q}.$$

Since $\sigma_{tot}(\gamma^* p) = (4\pi\alpha/Q^2)F_2$, this means that the total cross section at a fixed Q^2 is portional to W. Fig.19 shows the measured total cross sections multiplied by Q^2 as a function of W. The rise of the total cross section with W is in contrast to that of the total cross section for real photoproduction reactions at $Q^2 = 0$. It is also unlike the total $p\bar{p}$ cross section which is described by a term proportional to $W^{0.16}$ [10].

3.2 Charged current events

The diagram for charged current (CC) interactions of lowest order in deep ineslastic electron proton scattering is shown in fig.20 :

$$e^- + p \rightarrow \nu + X.$$

The exchanged current is the charged vector boson W. The scattered lepton in the final state is a neutrino which leaves the detector unobserved. Therefore the total transverse momentum p_t of the visible particles in the detector is not balanced, i.e. there is a missing p_t^{miss}. For these events, x and Q^2 must be calculated from the measured hadronic final states.

ZEUS studied the production of charged current events in a data sample corresponding to an integrated luminosity of 550 nb^{-1} requiring $Q^2 > 400$ GeV^2 and a missing transverse momentum $p_t^{miss} > 12$ GeV/c. In the data sample 22 charged currents events were found [37]. This results in the cross section data shown in fig.21 as a function of Q^2. Also shown are the neutral current cross section measured simultaneously by ZEUS and the prediction of the Standard Model. The dotted curve shows the prediction for $M_W \rightarrow \infty$.

Because of the high mass of the W boson, the CC cross section at low Q^2 is much smaller than for NC reactions. However one sees for the first time that, when Q^2 is of the order of the mass squared of the W, the weak interaction becomes as strong as the electromagnetic one. The prediction for the CC cross section with the standard W mass $M_W = 80.2$GeV agrees well with the data while the prediction for $M_W \rightarrow \infty$ is ruled out by the data. It becomes comparable only at $Q^2 \approx M^2_W$. At HERA, it has been observed for the first time that at Q^2 of about 10^4 GeV^2 the charged current cross section is of the same magnitude as the neutral current one. The agreement of the data with the Standard Model implies the presence of the the weak propagator with a finite W mass.

4 Large Rapidity Gap Events

Fig.22a shows a standard neutral current DIS event in the ZEUS detector. The scattered electron is detected in the high resolution calorimeter. There is hadronic activity in the central region of the calorimeter as well as close to the proton direction. The underlying process is sketched in fig.22b. The hadronic final state originates from fragmentation of the struck quark, of the proton remnant, and from initial and final state QCD radiation. ZEUS observed a new class of events in deep inelastic scattering [38], an example of which is shown in fig.23a. The underlying process is sketched in fig.23b. No hadronic activity close to the proton direction is detected. The first particle or energy deposit in the calorimeter is seen under a larger angle, i.e. at small pseudorapidity. Such events show a rapidity gap between the edge of the calorimeter in forward direction and the closest hadronic activity at $\eta = \eta_{max}$, where η_{max} is the largest pseudorapidity of any cluster with at least 400 MeV energy.

The distribution of η_{max} for all DIS events is presented in fig. 24. The obvious feature of the data is an excess of events at low η_{max} values that cannot be described by a model which contains only the standard DIS processes. A scatter plot of W vs. η_{max} for all events, as given in fig.25a, demonstrates that there is a distinct class of events with $\eta_{max} < 1.5$. This is confirmed by a scatter plot of the measured hadronic mass M_x vs. W in fig.25b. Events with $\eta_{max} < 1.5$ have small hadronic masses M_x and are clearly distinct from those with $\eta_{max} > 1.5$. Their M_x distribution is shown in fig. 26. The invariant masses of the detected final states of large rapidity gap (LRG) events, defined by $\eta_{max} < 1.5$, are considerable smaller than those

for standard DIS events. In fig.27 the ratio of the number of detected LRG events to all DIS events is plotted as a function of W. Also shown is the acceptance of the detector for DIS events. Above $W = 140$ GeV, where the acceptance is approximately independent of W, the ratio is about constant. This means that the W dependence of LRG events is similar to that of standard DIS events, at least at higher W values. Fig.28a-c show the Q^2 dependence of the ratio of LRG events to all events for $W > 140$ GeV in three different x intervals. This ratio is essentially flat, meaning that the Q^2 depence of LRG events is the same as that of standard DIS events. Since deep inelastic scattering is a leading twist process one consequently has to conclude that the underlying mechanism which produces LRG events is also a leading twist process.

In LRG events, the proton did not fragment into a visible system of hadrons. However, it can have dissociated into a system which is closely confined to the proton direction thereby avoiding detection. Also, no appreciable amount of initial state QCD radiation can have taken place since it would have resulted in hadrons detectable in the forward calorimeter. The most natural explanation for LRG events is the emittance of a color neutral particle from the proton which interacts with the exchanged virtual photon to form a hadronic system of mass M_x.

4.1 What is the mechanism for the production of LRG events ?

Large rapidity gaps in events are known to occur in peripheral processes if the center of mass energy of the reaction is much larger than the masses of involved particles (systems).

Peripheral processes are described by Reggeon exchange which gives rise to the following dependence of the cross section on the center of mass energy squared s :

$$\sigma_R \sim \left(\frac{s}{M_0^2}\right)^{2\alpha_R(0)-2} .$$

Here M_0 is some reference mass and $\alpha_R(0)$ is the intercept of the trajectory of Reggeon R at $t = 0$, where t is the four momentum transfer squared to the proton or target particle. Note that in the case of DIS LRG events $s = W^2_{\gamma^* p}$. The intercepts and the expected s dependences of cross sections for Regge trajectories are :

R	$\alpha_R(0)$	σ_R
π	0	$\sim s^{-2}$
ρ	$\frac{1}{2}$	$\sim s^{-1}$
IP	≈ 1	$\approx$ constant

Here IP is the Pomeron trajectory. The Pomeron was invented as a hypothetical particle to describe diffractive processes. At higher $W_{\gamma^* p}$ values, the contributions from the pion and rho trajectories will have vanished because of their steeply falling contribution to the cross section. Experimentally one finds that the fraction of LRG events stays approximately constant at high W, as seen in fig.27. This suggests that LRG events are produced by diffractive-like processes.

ZEUS has compared the data with two Monte Carlo programs which are available to simulate the production of LRG events. One is the Nikolaev-Zakharov (NZ) model [39] and the other one the POMPYT model [40]. The Nikolaev-Zakharov model describes Pomeron exchange essentially by the splitting of the virtual photon into a quark-antiquark pair which interacts with a colorless system of two gluons emitted from the proton, as shown in fig.29.

The POMPYT program is based on the Ingelmann-Schlein model [41] which was developed to describe diffractive processes in $p\bar{p}$ scattering observed by UA8 [42]. It assumes a partonic structure of the Pomeron. The virtual photon couples to one of the quarks(antiquarks) inside the Pomeron, as shown in fig.30. The histograms in fig.25 and fig.27 refer to these NZ and POMPYT Monte Carlo simulations. Both models give a reasonable description of the main features of the data.

4.2 Hard scattering and jets in LRG events

If LRG events are due to Pomeron exchange processes and the Pomeron has a partonic structure, then jet production should show up for a certain fraction of these events. In fig.31 one possibility for two jet production by Pomeron exchange is sketched. A parton in the pomeron undergoes a hard interaction with the virtual photon and produces two jets. ZEUS has looked for the production of jets in LRG events [43]. Fig.32 shows the pattern of energy deposits in the $\eta - \phi$ plane for such an event. The scattered electron and two jets are clearly visible. An analysis of jets in LRG events has been performed in the ep laboratory system and in the $\gamma^* p$ center of mass system. A jet was accepted if its transverse energy was $E_T > 4$ GeV in the ep-system and $E_T > 2$ GeV in the $\gamma^* p$-system. In fig.33a the measured transverse energy distribution of jets in the ep-system is presented. The transverse energy distribution of all LRG events in the $\gamma^* p$-system is given in fig.33b. The fractions of events with identified one, two, or three jets are indicated also. In the $\gamma^* p$-system the production of LRG events with total transverse energies above 7 GeV is saturated by hard processes leading to jet production. The presence of hard scattering processes supports the idea of a partonic structure of the Pomeron.

4.3 Outlook on diffractive scattering at ZEUS

LRG events are defined by the absence of energy deposition in the detector at the very forward direction. They are interpreted as diffractive processes originating from Pomeron exchange. For a detailed understanding of the diffractive processes it is important to isolate well defined final states, in particular at the nucleon vertex. In 1993, ZEUS has commissioned the leading proton spectrometer (LPS), which is a system of six stations of silicon strip detectors located in the HERA tunnel between 26 m and 96 m behind the interaction point in the proton direction. These stations can detect protons scattered under very small angles and provide a precise momentum measurement, $\Delta p/p < 1\%$. In 1994, the first data have been collected with the LPS in operation. With LPS tagged events, it will be possible to identify reactions of the type $ep \rightarrow epX$ where X results from diffractive dissociation of the virtual photon. In addition promissing results have been obtained for the detection of forward going neutrons with a prototype calorimeter installed at a distance of 106 m close to the proton beam line.

5 Summary

In this talk, results from the ZEUS experiment were presented on photoproduction, deep inelastic scattering, and large rapidity gap events in deep inelastic scattering.
In photoproduction the following data were presented and conclusions were drawn :

- The total photoproduction cross section shows a slow rise from $W = 20$ GeV to HERA energies. The energy dependence can be described by models based on Regge theory as well as by QCD inspired models.

- Data were presented for elastic vector meson production. Cross sections were given for ρ° and J/Ψ production.
- Inclusive charged particle transverse momentum distributions show that there is a hard component in γp scattering.
- The existence of direct and resolved photon processes has been demonstrated. Resolved processes dominate photoproduction at HERA.
- In resolved photon processes, the photon remnant has been identified. The photon remnant shows a behavior similar to quark or gluon jets.

For deep inelastic scattering the following results were found :

- The structure function F_2 has been measured down to x values of $4{\cdot}10^{-4}$ at $Q^2 \geq 8.5$ GeV^2. It shows a strong rise with decreasing x at all values of $Q^2 < 500$ GeV^2. The rise demonstrates an increase of the parton density in the proton as $x \to 0$. It can be described by parametrizations which include a gluon distribution which becomes singular as $x \to 0$, $xg \sim x^{-n}$, $n > 0$.
- The measured F_2 values show the predicted logarithmic scaling violations.
- The gluon momentum destribution of the proton was extracted from the scaling violations of F_2 at $Q^2 = 20$ GeV^2 for x values between $4 \cdot 10^{-4}$ and 10^{-2}. Compared to $x > 10^{-2}$, a substantial increase of the gluon momentum distribution is found at small x.
- A measurement of the charged current cross section up to Q^2 above 10^4 GeV^2 was presented. For the first time the weak interaction in deep inelastic scattering has been observed to have a strength comparable to that of electromagnetic interaction when $Q^2 \approx M_W{}^2$. The data agree with the standard model prediction.

A special class of events with a large rapidity gap has been detected. The presented results indicate that :

- Large rapidity gap events are a class of events separate from standard DIS events. They are characterized by missing energy deposition close to the proton direction. The mass of the hadronic system observed in the detector is small compared to standard DIS events. Their W and Q^2 dependences are the same as for standard DIS events. This leads to the conclusion that their production mechanism is diffractive-like and a leading twist process.
- Hard scattering processes with jet production occur in LRG events. This supports the hypothesis of a partonic structure of the Pomeron as seen in LRG events.

References

[1] ZEUS Collab., M.Derrick et al., Phys.Lett. B293 (1992) 465 ; The ZEUS Detector, Status Report 1993, DESY 1993 .

[2] C.Alvisi et al., Nucl.Instr. and Meth. A305 (1991) 30 .

[3] C.B.Brooks et al., Nucl.Instr. and Meth. A283 (1989) 477 ; B.Foster et al., Nucl.Instr. and Meth. A338 (1994) 254 .

[4] A.Andresen et al., Nucl.Instr. and Meth. A309 (1991) 101 ; A.Bernstein et al., Nucl.Instr. and Meth. A336 (1993) 23 ; A.Caldwell et al., Nucl.Instr. and Meth. A321 (1992) 356 .

[5] D.Kisielewska et al., Fast Luminosity Monitoring at HERA, DESY-HERA report 85-25 ; J.Andruszkow et al., DESY 92-066 (1992) .

[6] J.J.Sakurai, Ann.Phys. 11 (1960) 1 ; T.H.Bauer et al., Rev.Mod.Phys. 50 (1978) 261 .

[7] ZEUS Collab., M.Derrick et al., Z.Phys C63 (1994) 391 .

[8] H1 Collab., T.Ahmed et al., Phys.Lett. B299 (1993) 374 .

[9] D.O.Caldwell et al., Phys.Rev.Lett. 40 (1978) 1222 ; S.I.Alekhian et al., CERN-HERA 87-01 (1987) .

[10] A.Donnachie and P.V.Landshoff, Nucl.Phys. B244 (1984) 322 ; Z.Phys. C61 (1994) 139 ; P.V.Landshoff, Nucl.Phys. B(Proc.Suppl.) 18C (1990) 211 .

[11] H.Abramowicz, E.M.Levin, A.Levy, and U.Maor, Phys.Lett. B209 (1991) 465 .

[12] M.Drees and F.Halzen, Phys.Rev.Lett. 61 (1988) 275 ; R.Ghandi and I.Sarcevic, Phys.Rev. D44 (1991) R10 ; J.R.Forshaw and J.K.Storrow, Phys.Lett. B268 (1991) 116 ; R.S.Fletcher, T.K.Gaissner, and F.Halzen, Phys.Rev. D45 (1992) 377 .

[13] ZEUS Collab., M.Derrick et al., contributed paper ICHEP Ref. 0688, Glasgow July 1994 ; ZEUS Collab., M.Derrick et al., contributed paper ICHEP94 Ref. 0672, Glasgow July 1994 ; A.Proskuryakov, Talk at the Workshop 'The Heart of the Matter', Blois, France, June 1994 .

[14] S.D.Holmes,W.Lee, and J.E.Wiss, Ann.Rev.Nucl.Part.Sci. 35 (1985) 397 ; A.Baldini et al., Landolt-Börnstein, Group I, Vol.12b, Springer-Verlag, ed. H.Schopper .

[15] ZEUS Collab., M.Derrick et al., contributed paper ICHEP94 Ref. 0690, Glasgow 1994 .

[16] ZEUS Collab., M.Derrick et al., DESY 94-176 .

[17] J.Huth et al., Proc. 1990 DPF Summer Study on High Energy Physics, Snowmass, Colorado, ed. E.L.Berger, World Scientific, Singapore 1992, p.134 .

[18] A.D.Martin,W.J.Stirling, and G.R.Roberts, Phys.Rev. D47 (1993) 867 .

[19] M.Glück,E.Reya, and A.Vogt, Phys.Rev. D46 (1992) 1973 .

[20] H.Abramowicz,K.Charchula, and A.Levy, Phys.Lett. 268B (1991) 458.

[21] ZEUS Collab., M.Derrick et al., Phys.Lett. B322 (1994) 287 .

[22] ZEUS Collab., M.Derrick et al., contributed paper ICHEP Ref. 0684, Glasgow July 1994 .

[23] S.Bentvelsen,J.Engelen, and P.Kooijman, Proc. of the Workshop 'Physics at HERA' Vol.1, DESY 1992 ; S.Bentvelsen, PhD Thesis, University of Amsterdam 1994 .

[24] ZEUS Collab., M.Derrick et al., DESY 94-143 , to be published in Z.Phys. C .

[25] V.N.Gribov and L.N.Lipatov, Sov.Journ.Phys. 15 (1975) 438, 675 ; G.Altarelli and G.Parisi, Nucl.Phys. 126 (1977) 297 .

[26] A.D.Martin, R.G.Roberts, and W.J.Sterling, Phys.Lett. B306 (1993) 145 .

[27] CTEQ Collab., J.Botts et al., Phys.Lett. B304 (1993) 159 .

[28] M.Glück,E.Reya, and A.Vogt, Phys.Lett. B306 (1993) 391.

[29] M.Glück,E.Reya, and M.Stratmann, Dortmund preprint DO-TH 93/20.

[30] H1 Collab., I.Abt et al., Nucl.Phys. B407 (1993) 515 .

[31] NMC Collab., P.Amaudruz et al., Phys.Lett. 295B (1992) 159 .

[32] E665 Collab., A.Kotwal, Talk at the Workshop 'The Heart of the Matter', Blois, France, June 1994 .

[33] K.Prytz, Phys.Lett. B311 (1993) ; K.Prytz, Phys.Lett. B332 (1994) 393 .

[34] R.K.Ellis,Z.Kunszt, and E.M.Levin, Nucl.Phys. B420 (1994) 517 .

[35] ZEUS Collab., M.Derrick et al., DESY 94-192 .

[36] L.N.Lipatov, Sov.Journ.Nucl.Phys. 23 (1976) 338 ; Y.Y.Balitsky and L.N.Lipatov, Sov.Journ.Nucl.Phys. 28 (1978) 822 ; E.A.Kuraev,L.N.Lipatov, and V.S.Fadin, Sov.Phys.JETP 45 (1977) 199 .

[37] ZEUS Collab., Presented at the Int. Workshop on DIS and Related Subjects, Eilat, Israel, Feb. 1994 ; S.Nickel, PhD Thesis, University Hamburg, 1994 ; G.Wolf, DESY 94-178 .

[38] ZEUS Coll., M.Derrick et al., Phys.Lett. B315 (1993) 481 .

[39] N.N.Nikolaev and B.G.Zakharov, Z.Phys. C53 (1992) 331 ; A.Solano, PhD Thesis, University of Torino 1993 .

[40] P.Bruni and G.Ingelman, DESY 93-187 and Proc. of the Europhysics Conference, Marseille 1993 ; H.U.Bengtssen and T.Sjöstrand, Comp.Phys.Comm. 46 (1987) 43 ; T.Sjöstrand, CERN-TH 6488/92 .

[41] G.Ingelman and P.Schlein, Phys.Lett. B152 (1985) 256 .

[42] UA8 Collab., A.Brandt et al., Phys.Lett. B297 (1882) 417 .

[43] ZEUS Collab., M.Derrick et al., Phys.Lett. B332 (1994) 228 .

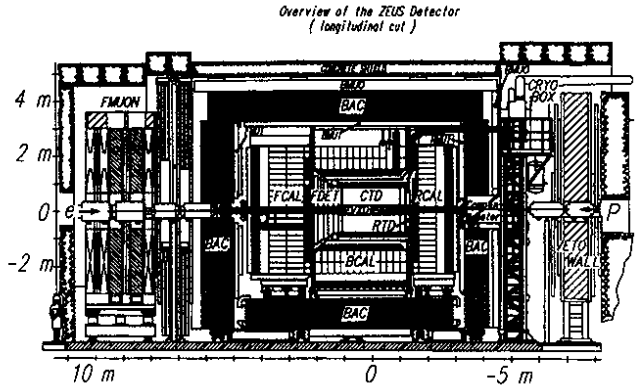

Fig.1 : Cross section through the ZEUS detector.

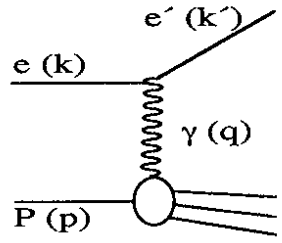

Fig.2 : A diagram for a photoproduction reaction.

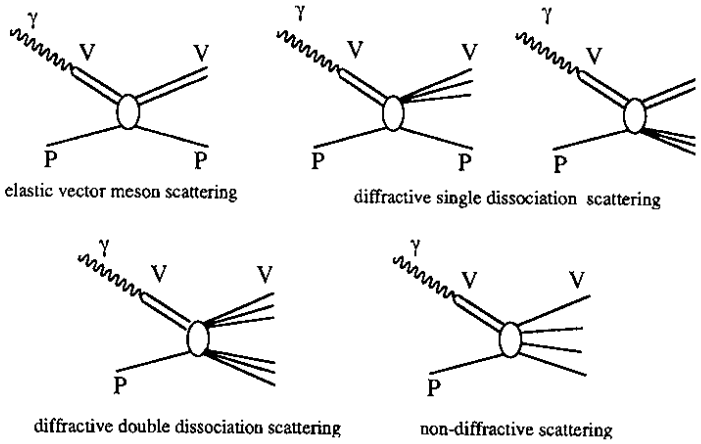

Fig.3: Diagrams for Vector Meson Dominance reactions.

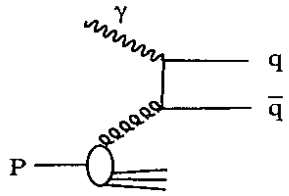

Fig.4a : Diagram for a direct photon process.

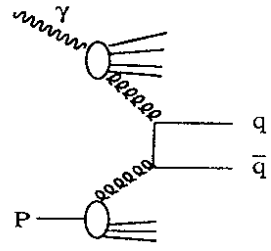

Fig.4b: Diagram for a resolved photon process.

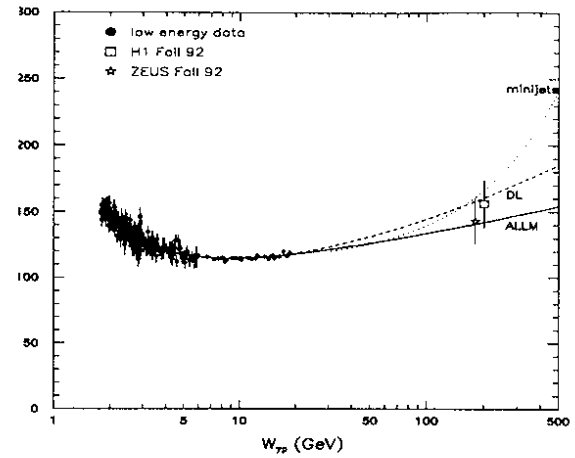

Fig.5 : The total photoproduction cross section as a function of the hadronic center of mass energy W.

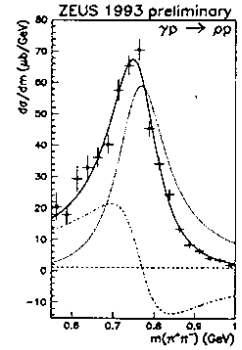

Fig.6a : The ρ signal with a mass fit including a Söding type interference term (dashed-dotted).

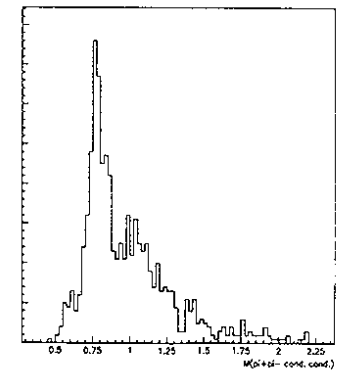

Fig.6b : Invariant mass spectrum of two charged pions plus one neutral pion.

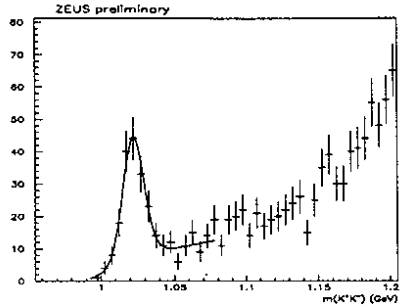

Fig.6c : Invariant mass spectrum of two charged kaons.

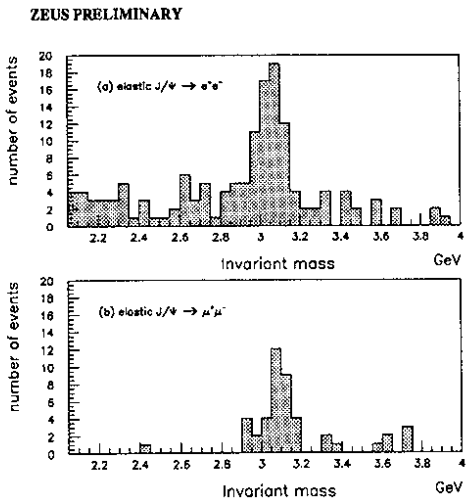

Fig.6d : Invariant mass spectra for e^+e^- pairs and $\mu^+\mu^-$ pairs in the mass region 2-4 GeV.

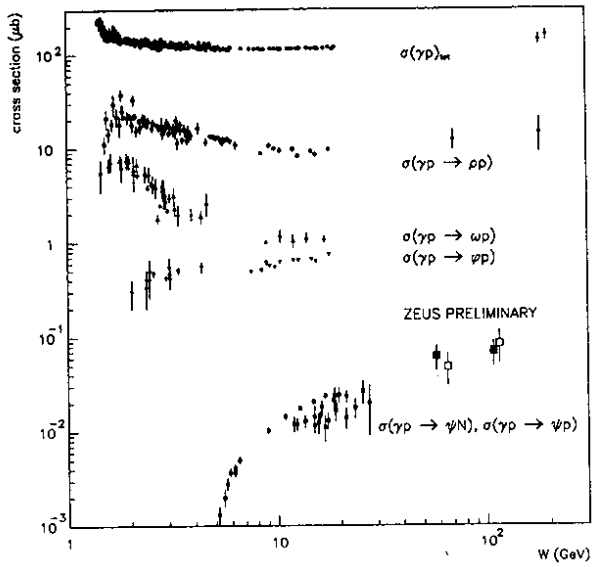

Fig.7 : Total photoproduction and vector meson production cross sections.

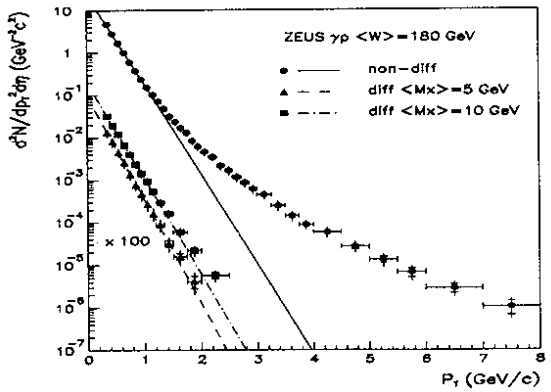

Fig.8 : Inclusive charged paricle transverse momentum spectra for photoproduction reactions.

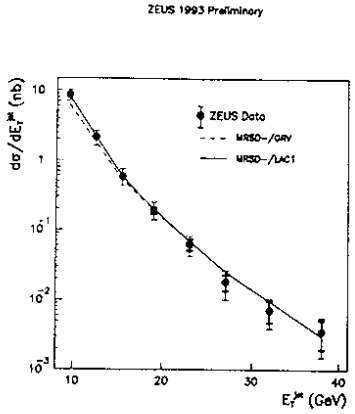

Fig.9a : Distribution of transverse jet momenta in photoproduction events.

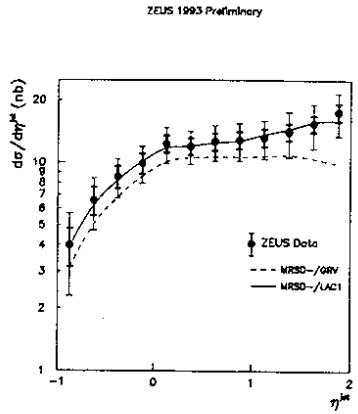

Fig.9b : Rapidity distribution of jets in photoproduction events.

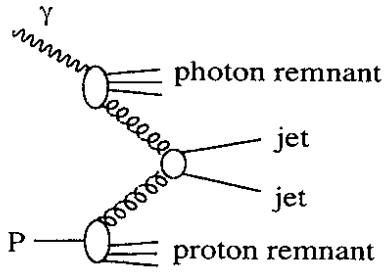

Fig.10 : A diagram for a resolved photon interaction.

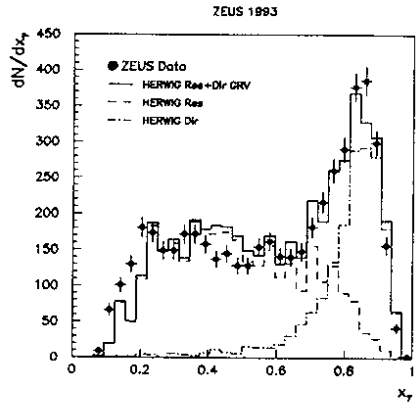

Fig.11 : Distribution of measured x_γ values.

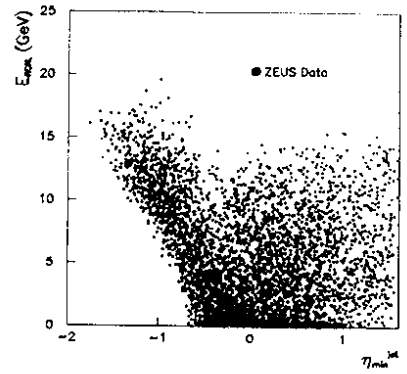

Fig.12 : Energy measured in the rear calorimeter versus rapidity of the most backward going jet.

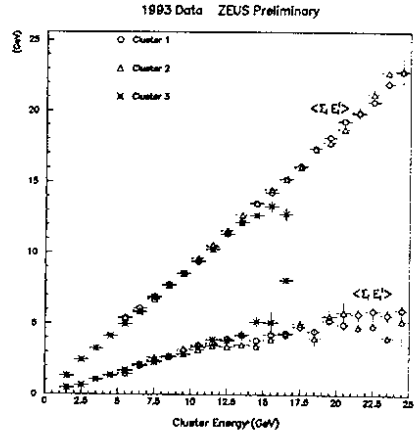

Fig.13 : Average longitudinal and transverse cluster energies as functions of the cluster energies.

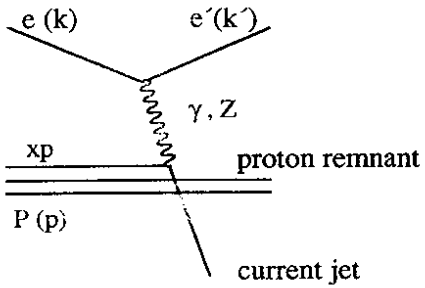

Fig.14 : Diagram for neutral current deep inelastic scattering in lowest order.

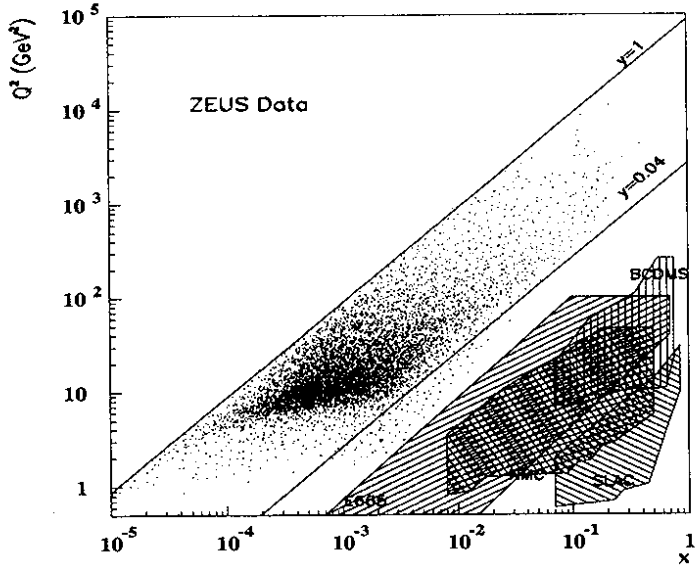

Fig.15 : Kinematical regime of ZEUS DIS data and other experiments.

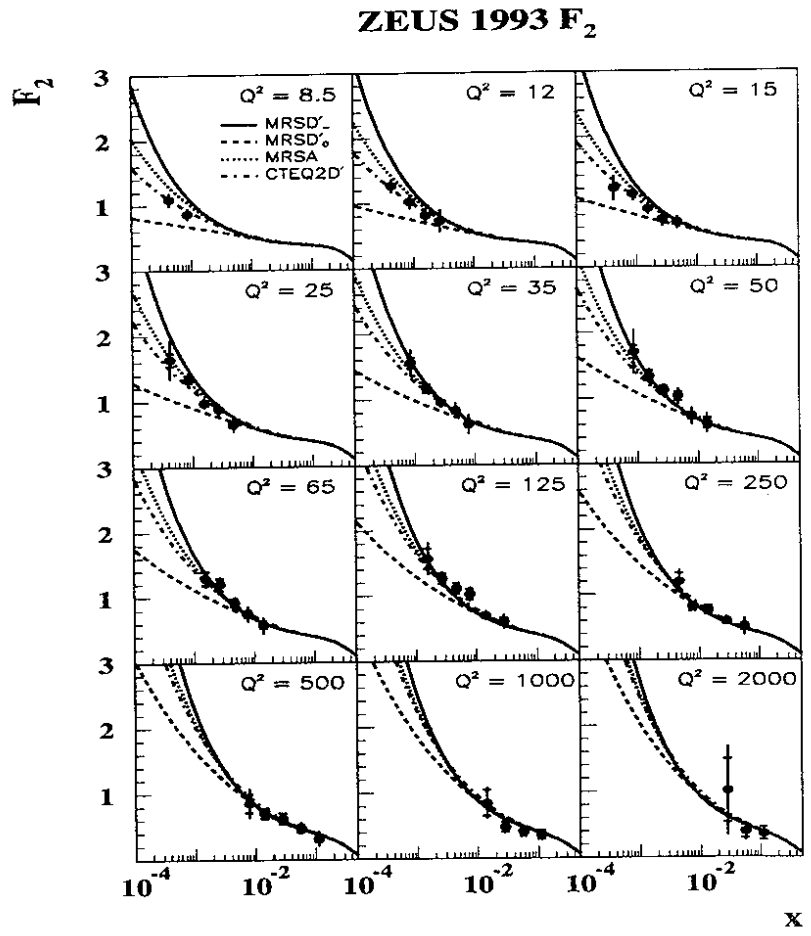

Fig.16a : F_2 data from ZEUS as functions of x for different Q^2 values compared to several parametrizations, see text.

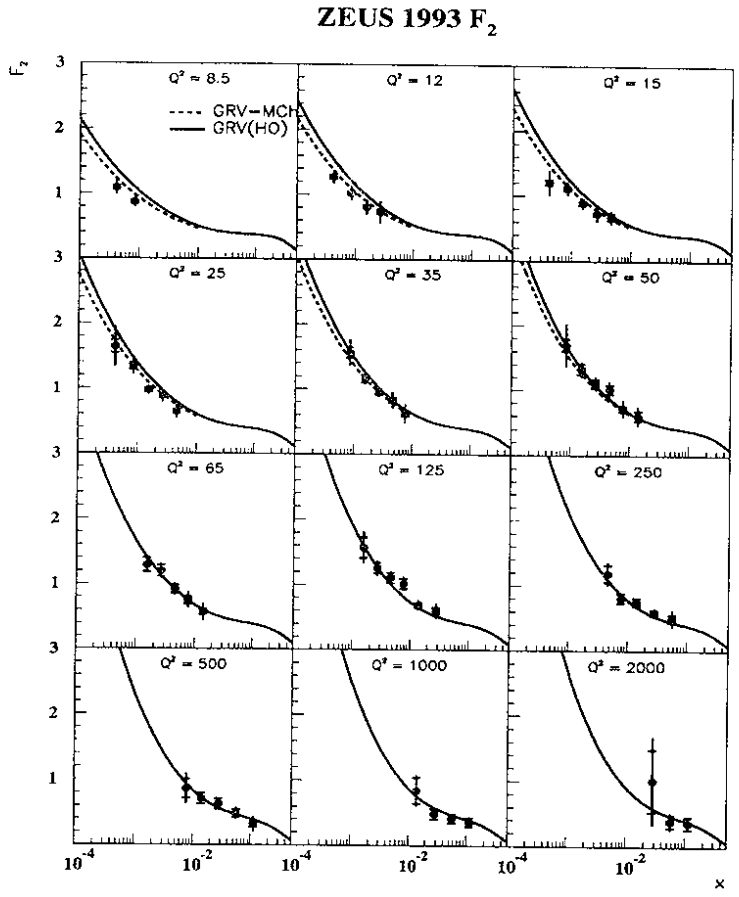

Fig.16b: F_2 data from ZEUS as functions of x for different Q^2 values compared to several parametrizations, see text.

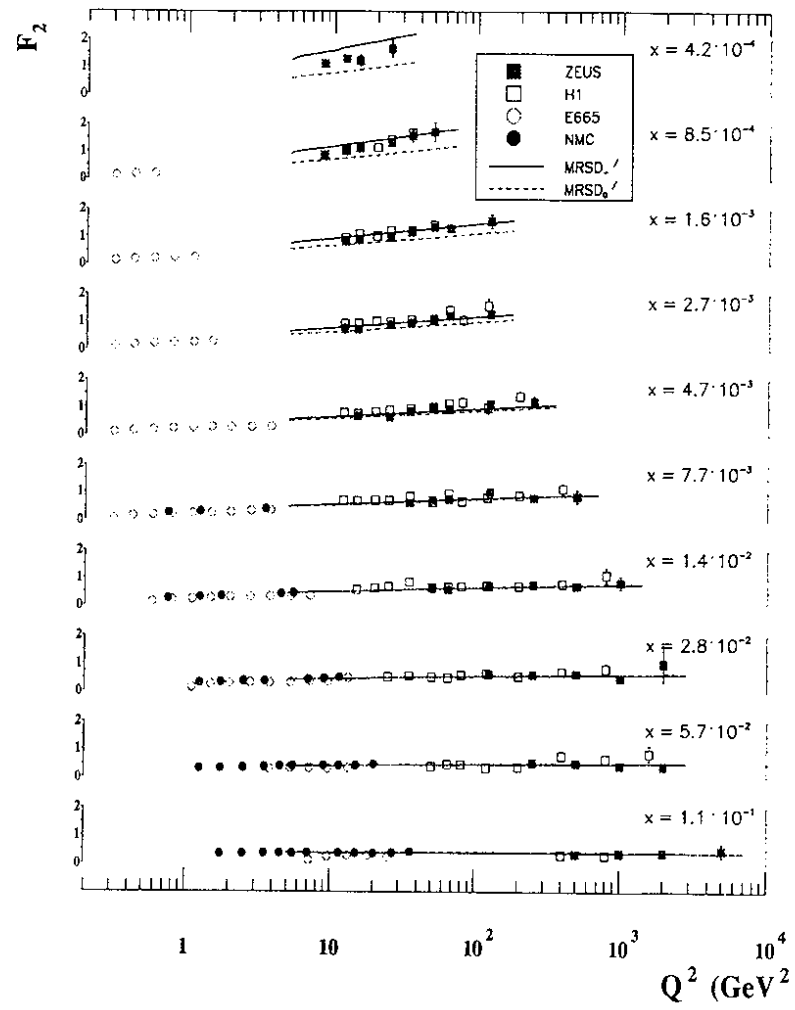

Fig.17 : F_2 as a function of Q^2 at different x values.

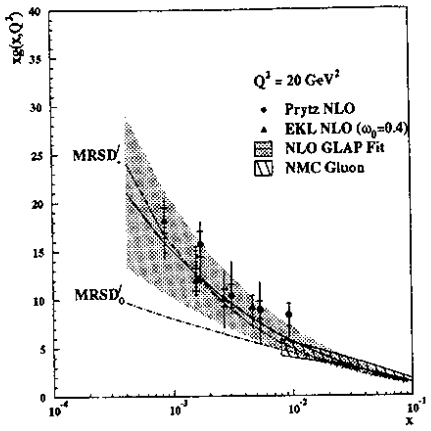

Fig.18: The gluon momentum distribution as determined from the ZEUS data.

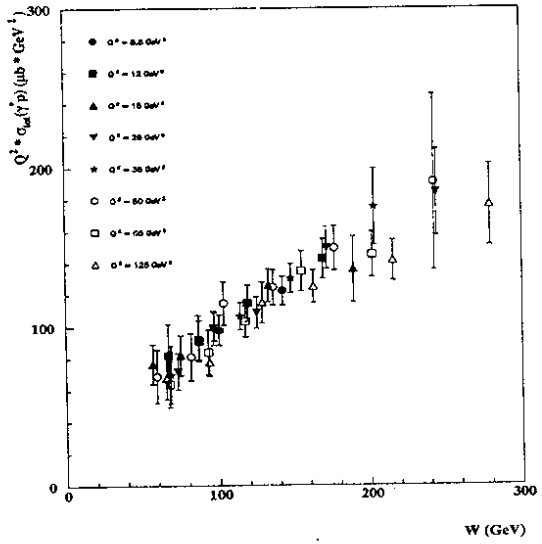

Fig.19 : Total $\gamma^* p$ cross section multiplied by Q^2 as a function of W.

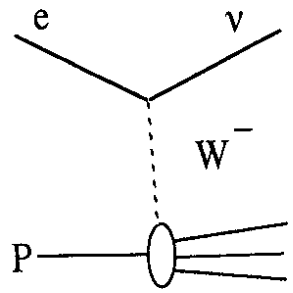

Fig.20 : Diagram for charged current deep inelastic scattering in lowest order.

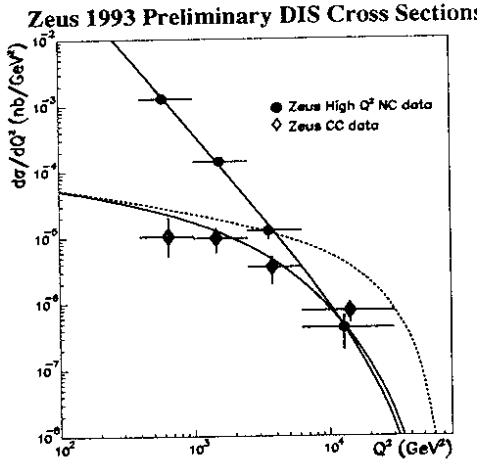

Fig.21 : Charged current and neutral current cross sections at high Q^2 together with Standard Model predictions. The dotted line is the prediction for $M_W \to \infty$.

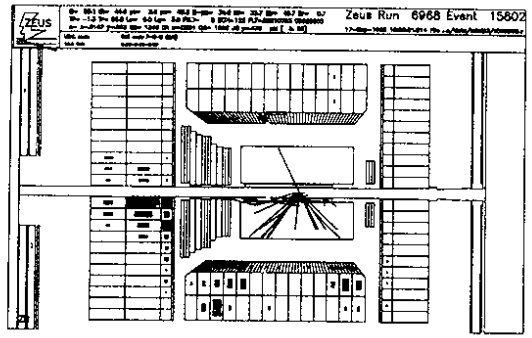

Fig.22a : Event picture of a normal DIS event.

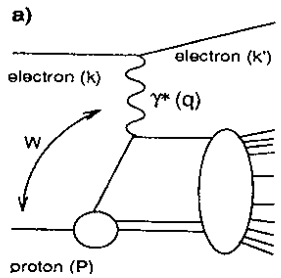

Fig.22b : Diagram for standard deep inelastic scattering.

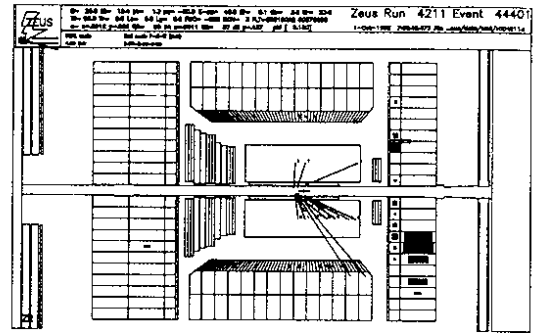

Fig.23a : Event picture of a large rapidity gap event event.

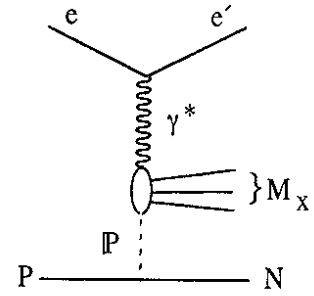

Fig.23b : Diagram of a process leading to large rapidity gap events. N denotes either a proton or a diffractively excited state of the proton.

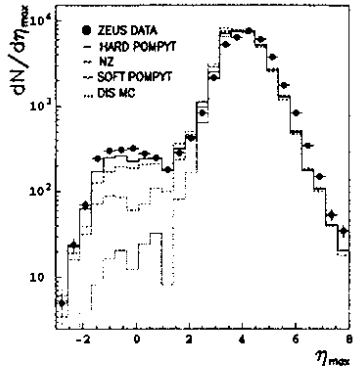

Fig.24: Distribution of η_{max} for DIS events.

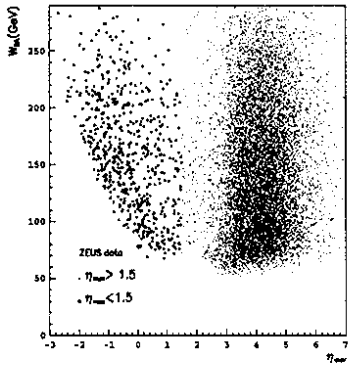

Fig.25a: W versus η_{max} for DIS events.

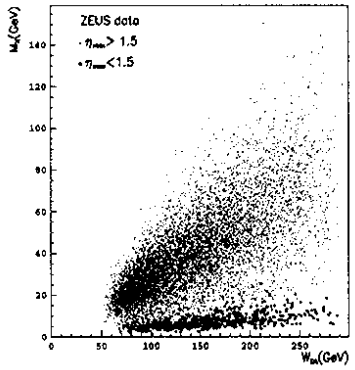

Fig.25b: Hadronic mass versus W for DIS events.

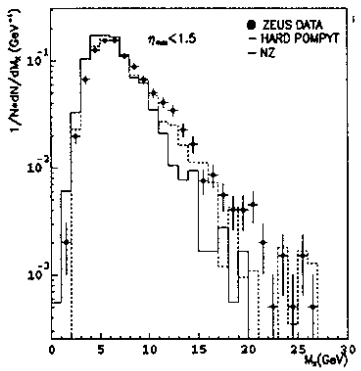

Fig.26: Distribution of hadronic masses for large rapidity gap events.

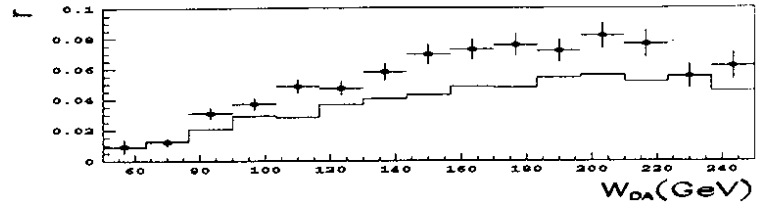

Fig.27 : Ratio r of events with $\eta_{max} < 1.5$ to all DIS events. The solid line indicates the detector acceptance.

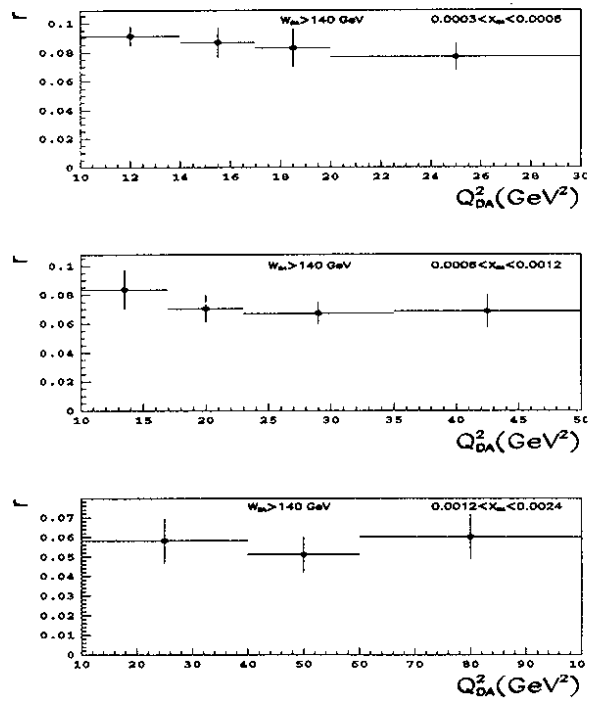

Fig.28 : Ratio r of events with $\eta_{max} < 1.5$ to all DIS events for $W > 140$ GeV as a function of Q^2 for $0.0003 < x < 0.0006$, $0.0006 < x < 0.0012$, and $0.0012 < x < 0.0024$.

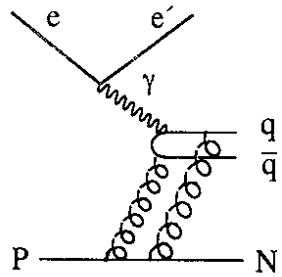

Fig.29 : Pomeron exchange in the Nikolaev-Zakharov model. N denotes either a proton or a diffractively excited state of the proton.

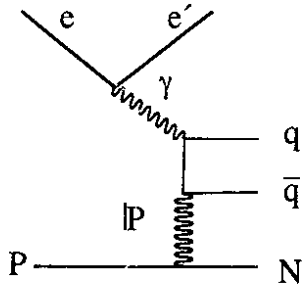

Fig.30 : Pomeron exchange in the Pompyt model. N denotes either a proton or a diffractively excited state of the proton.

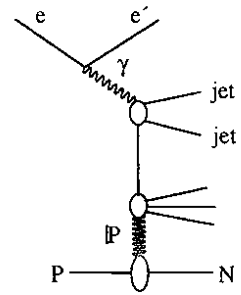

Fig.31 : Two jet production by pomeron exchange. N denotes either a proton or a diffractively excited state of the proton.

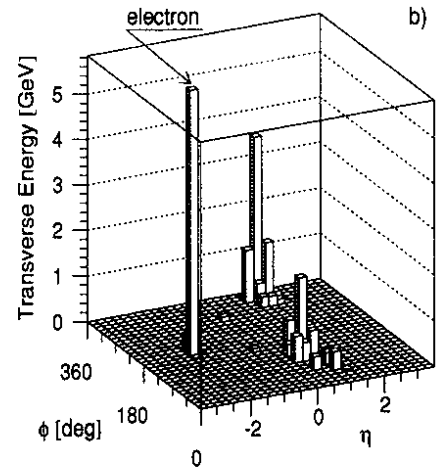

Fig.32 : A large rapidity gap two-jet event.

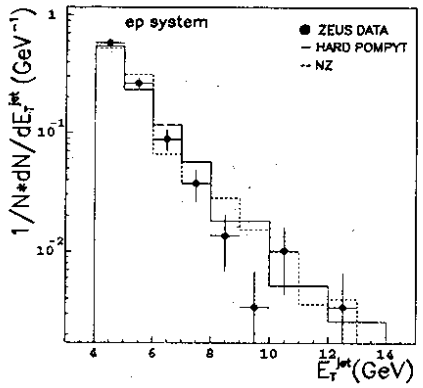

Fig.33a : The jet transverse energy distribution in the laboratory system for large rapidity gap events.

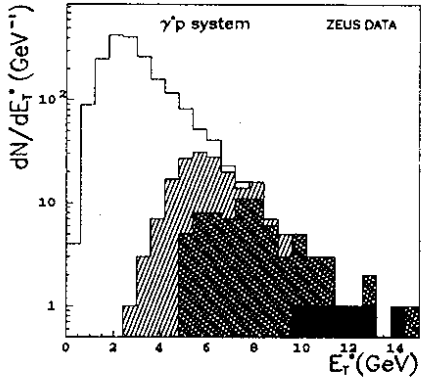

Fig.33b : The total hadronic energy transverse to the virtual photon direction for large rapidity gap events (hashed : 1-jet events ; cross hashed : 2-jet events ; solid : 3-jet events).